2021 IEEE International Conference on Communications Workshops (ICC Workshops) | 978-1-7281-9441-7/20/$31.00 ©2021 IEEE | DOI: 10.1109/ICCWorkshops50388.2021.9473566

Double-Directional Channel Measurements for Urban THz Communications on a Linear Route

Naveed A. Abbasi*, Jorge Gomez-Ponce*†, Daoud Burghal*, Revanth Kondaveti*,
Shadi Abu-Surra‡, Gary Xu‡, Charlie Zhang‡, Andreas F. Molisch*
* University of Southern California, Los Angeles, CA, USA
†ESPOL Polytechnic University, Escuela Superior Politécnica del Litoral, ESPOL,
Facultad de Ingeniería en Electricidad y Computación, Km 30.5 vía Perimetral, P. O. Box 09-01-5863, Guayaquil, Ecuador
‡ Samsung Research America, Richardson, TX, USA
Email: {nabbasi, gomezpon, burghal, kondavet, molisch}@usc.edu,
{shadi.as, gary.xu, jianzhong.z}@samsung.com

***Abstract*—The large swaths of bandwidth available in the THz band (0.1-10 THz) make it an ideal candidate to meet the ever-increasing data rate demands for upcoming applications. However, detailed channel sounding measurements are required before an eventual deployment of THz band communication can be considered. Keeping this goal in mind, in the current paper we present double-directional channel measurements in the 140-141 GHz range in an urban environment on a linear route for distances up to 15 m. Using our results, we analyze how key channel parameters change as we move from short to longer distances. These measurements allow us to take another step towards creation of detailed THz channel models.**

***Index Terms*—Terahertz (THz) communication, urban scenario, double-directional channel measurements, linear route**

I. Introduction

Many recent and upcoming applications such as 3D virtual reality have such high data rate requirements that their deployment is beyond the capabilities of mmWave-based 5G communication networks [1]. This has motivated the wireless communication community to turn towards higher frequencies specifically in the THz band (0.1-10 THz) since large swathes of bandwidth in this band are currently unused. Many recent studies have explored 0.1-0.5 THz ([2]–[8]) in more detail since this portion of the THz band is envisioned to be a part of 6G wireless systems [9].

Communication in the THz band faces a number of challenges in terms of higher isotropic path loss and shadowing. Moreover, while the path loss may seem large, higher frequencies allows us to pack a larger number of antennas in a reasonable form factor thereby allowing higher antenna gains. Apart from these effects, the propagation characteristics of THz band are not well known since they are highly dependant on the environment the signals traverse through. Therefore, in order to properly analyze the band a large number of channel measurements are needed in various key application scenarios. By allowing experimental licenses in low-THz band, Federal Communication Commission (FCC) is trying to encourage further exploration of the THz band by means of channel measurements [10].

Most existing measurement-based studies in the THz communication are concentrated on short-range indoor scenarios ($\leq$5 m) [8], [11]–[14]. Extensions to larger ranges, which are in particular of interest for outdoor hotspots and picocells, have been hampered by limitations of the measurement equipment. Using a custom frequency-domain setup, we were able to conduct the first double-directional channel measurements over much larger distances (around 100 m) in the THz band [15] and explored several further outdoor device-to-device channels in our subsequent study [16]. Both of these papers used quasi-randomly located transmitter (Tx) and receiver (Rx) to investigate environments with specific properties, e.g., vegetation scattering, or reflections from building structures. In contrast, the current paper leaves the Tx at a fixed location and moves the Rx on a linear route to investigate the changes of propagation effects and channel properties as a function of distance *in the same outdoor urban environment*. More specifically, we conduct 4 *double-directional* measurements with distances of 1 m, 2 m, 5 m and 15 m between Tx and Rx. Furthermore, we also conducted the measurements with 3 different elevations at each measurement point to see how the multipath environment changes with elevation differences. We analyze our measurements in terms of angular power spectrums (APSs), power delay profiles (PDPs), as well as path loss and multipath component (MPC) richness.

The rest of this paper is organized as follows. The measurement setup and site are described in Section II. Section III highlights our major results for the current measurement campaign. The manuscript is finally concluded in Section IV.

II. Measurement equipment and site

A. Testbed description

Our current work is based on a frequency-domain setup that is shown in Fig. 1. The basic principle of this channel sounder revolves around frequency extension of a vector network analyzer (VNA) signal into the THz domain by means of frequency multipliers. We use a RF-over-fiber (RFoF) connection between VNA and frequency extender to allow the placement of the Rx beyond the distance limitations of a typical VNA-based THz channel sounding system ($<$ 10 m). This design is similar to the one discussed in our previous work [15] with the difference being that we currently use an

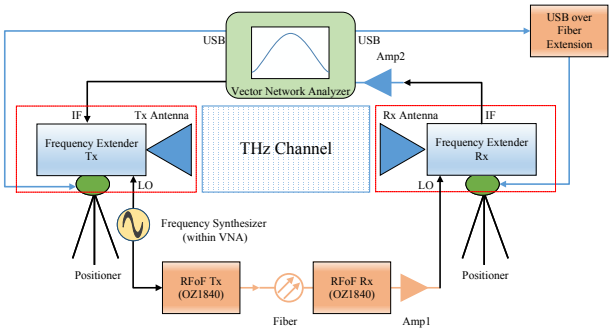

Fig. 1: Channel sounding setup.

integrated RFoF unit to improve the robustness of the design. We use time-gated over-the-air (OTA) calibrations to calibrate the system.

Both Tx and Rx use horn antennas to enhance the SNR and at the same time limit the MPCs to a particular angular range; mechanical rotation of the horn antennas provides the double-directional channel characteristics, i.e., the transfer function (or impulse response) for each combination of Tx and Rx direction [17]. Due to the measurement principle of mechanically rotating antennas, every measurement lasted for several hours; measurements were done at night to ensure that no movement of people or vehicles was present in the environment. Further details about the setup can be found in [15].

B. Site description

As discussed earlier, the chosen scenario and the environmental characteristics are themselves a very important factor in any channel sounding campaign. For the current measurement, we investigate an outdoor urban scenario. Specifically, our environment is located at the entrance of the Vivian Hall of Engineering (VHE) building on the USC University Park Campus, Los Angeles, CA, USA. It is an open space area with interspersed pillars (see Fig. 2). There are concrete walls and glass doors towards the North and South of the measurement area. The East side faces low height buildings and a wide street while the West side faces an open area (quad) with several chairs, tables, trees, and a water fountain at a distance of around 50m from the measurement area (this is the side shown in Fig. 2 (b)).

The reported campaign consisted of 4 measurements on a linear route with a fixed Tx and Rx at various distances up to 15 m (Fig.2). For all links, the height of the Tx and Rx was fixed at 1.65 m to emulate typical device-to-device (D2D) communication links. Both the Tx and Rx were placed on paved ground.

C. System configuration

For this experiment, the measurement parameters, acronyms and nominal values are described in Table I. The number of frequency points per sweep is 1001 over the 1 GHz bandwidth resulting in 1 MHz of frequency resolution, 1μs of maximum excess delay or 300 m of maximum measurable distance.

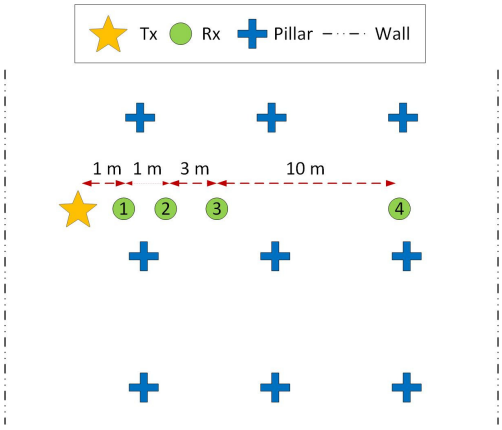

(a) Site map.

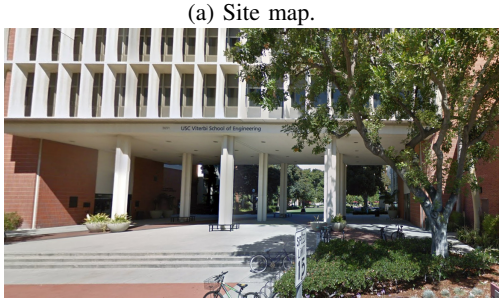

(b) Site image.

Fig. 2: Measurement scenario description.

TABLE I: Setup parameters.

Parameter	Symbol	Value
Measurement points	N	1001
Tx/Rx height	$h_{Tx/Rx}$	1.65 m
Tx/Rx LoS distance	$d_{Tx/Rx}$	[1,2,5,15]
Start frequency	f_{start}	140 GHz
Stop frequency	f_{stop}	141 GHz
Bandwidth	BW	1 GHz
IF bandwidth	IF_{BW}	10 KHz
THz IF	f_{THzIF}	279 MHz
Antenna 3 dB beamwidth	θ_{3dB}	13°
Tx rotation range	Tx_{AZ}	[0°,360°]
Tx rotation resolution	ΔTx_{AZ}	10°
Rx Az rotation range	Rx_{AZ}	[0°,360°]
Rx Az rotation resolution	ΔRx_{AZ}	10°
Rx El rotation range	Rx_{EL}	[80°,100°]
Rx El rotation resolution	ΔRx_{EL}	10°

Given the scenario, the maximum distance is enough to capture the channel behavior.

The positioners (rotors) were set such that the angle of 0° for both the Tx and the Rx corresponds to the line of sight (LoS) for all points over the route. The Tx scans over a single elevation cut ($\phi_{Tx} = 90°$; $\phi_{Tx} = 0°$ is defined to be in the zenith) from 0° to 360° with a 10° angular resolution. For the Rx, three elevations cuts ($\phi_{Rx} = 80°, 90°, 100°$; $\phi_{Rx} = 0°$ is again defined to be in the zenith) are taken and at each of these elevations a full azimuth scan is done similar to Tx. Since we have a single elevation cut at the Tx, the use of term ϕ_{Tx} is redundant and is therefore not used further.

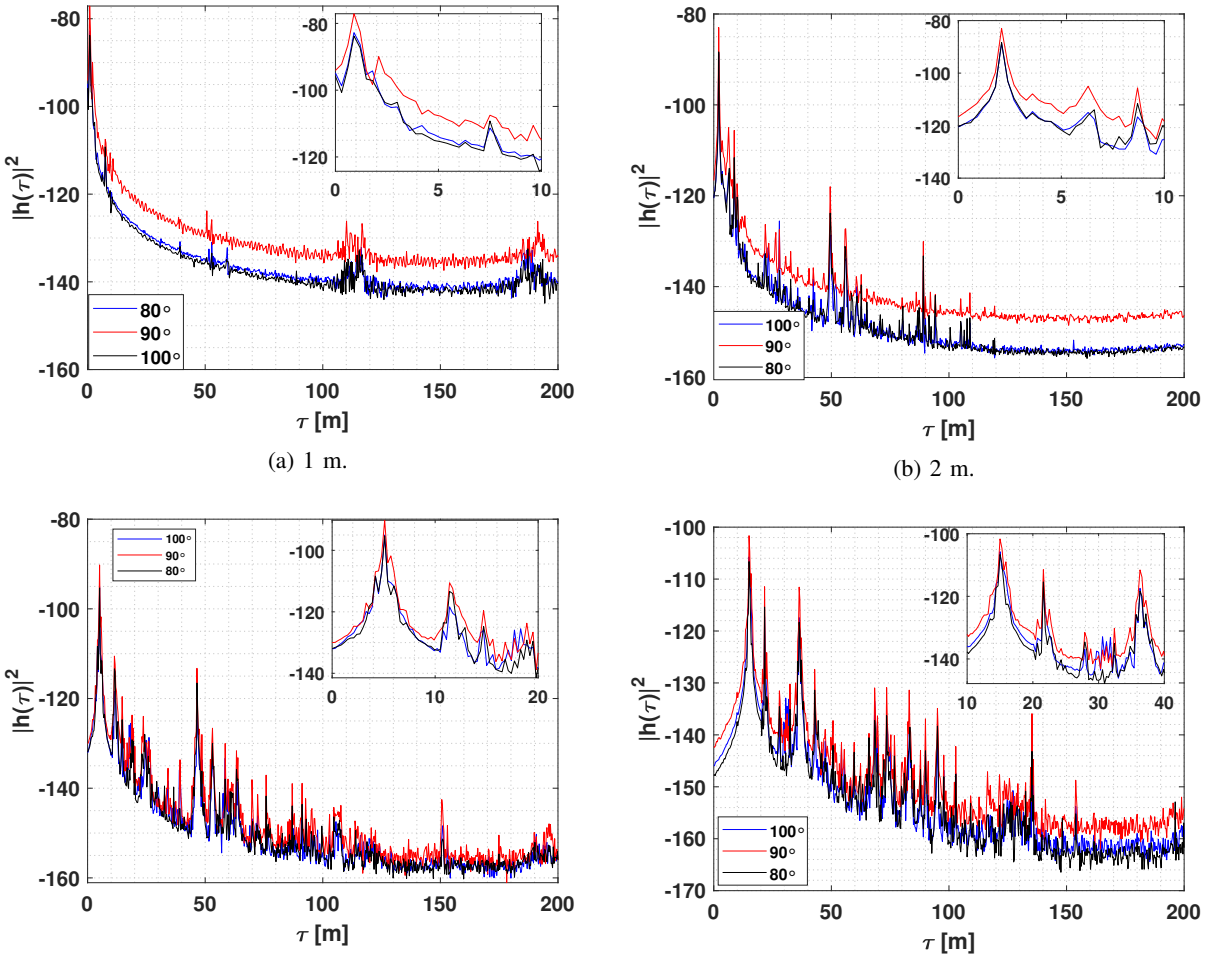

(a) 1 m.

(b) 2 m.

(c) 5 m.

(d) 15 m.

Fig. 3: Omni-directional PDPs for different elevations.

III. Measurement Results

Before moving on to analyze the results, we define some of the key terms used herein. A calibrated (using the OTA calibration) "directional" channel frequency response is denoted as $H(f, \theta_{Tx}, \theta_{Rx}, \phi_{Rx})$. Directional PDP for each direction is computed as

$$P(\tau, \theta_{Tx}, \theta_{Rx}, \phi_{Rx}, d) = |\mathcal{F}_f^{-1}\{H(f, \theta_{Tx}, \theta_{Rx}, \phi_{Rx}, d)\}|^2, \quad (1)$$

where $\mathcal{F}_f^{-1}$ represents Inverse Fast Fourier Transform (IFFT) with respect to f, θ_{Tx} is the Azimuth direction for Tx horn, θ_{Rx} is the Azimuth direction for Rx horn, ϕ_{Rx} is the Elevation angle for Rx horn, and d is distance between Tx and Rx. As a final processing step, noise and delay gating is applied to the PDP when calculating additional parameters similar to [18]. Here, τ_{gate} is set to 666.67 ns (i.e. 200 m) and for P_λ we set the value to be 6 dB above the noise floor of the PDP.

To observe the channel behavior from an "omni-directional" perspective, we reconstruct the omni-directional pattern from a MIMO capture by selecting the direction of the highest contribution per delay bin similar to [16], [19] as

$$P_{\text{omni}}(\tau, \phi_{Rx}, d) = \max_{\theta_{Tx}, \theta_{Rx}} P(\tau, \theta_{Tx}, \theta_{Rx}, \phi_{Rx}, d). \quad (2)$$

Using the functions previously described, we compute the root mean square (RMS) delay spread, angular spread and MPC power distribution as follow

1) The delay spread is calculated as the second central moment of the PDP [20]. Note that we can define a directional delay spread that is associated with a particular directional PDP, as well as an omni-directional delay spread that is derived from the reconstructed omni-directional PDP.
2) We compute the APS as
$$APS(\theta_{Tx}, \theta_{Rx}, \phi_{Rx}, d) = \sum_{\tau} P(\tau, \theta_{Tx}, \theta_{Rx}, \phi_{Rx}, d) \quad (3)$$
3) With the APS, we compute the angular spread by using Fleury's formula [21].
4) Using the omni-directional and the strongest beam directional PDPs for an specific distance d, we proceed to detect the major MPCs and sort them in descending

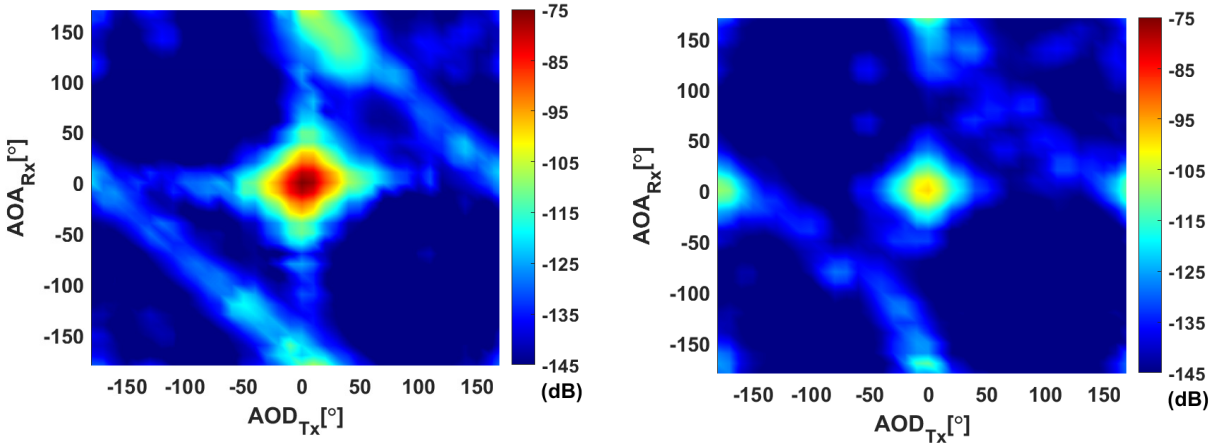

(a) 1 m.

(b) 15 m.

Fig. 4: Angular power spectrum for $\phi_{Rx} = 90°$.

order of power to analyze the percentage of power with respect to the total power of the PDP.

$$\gamma(K) = \frac{\sum_K P_i(\tau_K)}{\sum_\tau P_i(\tau)}, \tag{4}$$

where i can be omni-directional or the direction of the strongest power (Best beam). The numerator represents the power of the "K" strongest MPCs and the denominator is the total power of the PDP.

5) Using the omni-directional, directional PDP, the path loss is computed as follows:

$$PL_i(d) = \sum_\tau P_i(\tau, d), \tag{5}$$

where d is the distance between Tx and Rx.

The explained procedure was used for all points on the route.

A. Power delay profiles

The omni-directional PDPs for all the elevations and various distances are shown in Fig. 3. Looking at these, we make the following key observations:

- The major component in each case corresponds to the expected link distance, i.e., describes the LoS. This is an important test for the analysis and shows that the measurements and the sounding system are operating properly. The power for the major component decreases as the distance increases which is to be expected.
- $\phi_{Rx} = 90°$ has the highest power for the major component in all the cases. Since both Tx and Rx are at the same height, $\phi_{Rx} = 90°$ corresponds to the case where both the Tx and Rx are directly looking at each other. The difference is highest for $d =$ 1 m and $d =$ 2 m links since the beam is not as spread as is the case for $d =$ 5 m and $d =$ 15 m links.
- Multipath richness increases as the link length increases since the ratio for power of the major component with respect to other subsequent components decreases. Therefore, we see the highest number of components in the $d =$ 15 m case.

Apart from the LoS component, the other components in Fig. 3 correspond to the pillars and building structures in the environment. More can be said about their exact positioning by means of APS analysis.

B. Angular power spectrum

The APSs for $\phi_{Rx} = 90°$ for $d =$ 1 m and $d =$ 15 m links are shown in Fig. 4. In these figures, we see that for both the cases the strongest components are received around the LoS with higher power for the 1 m cases which is expected from Fig. 3 as well. Apart from the LoS, strong reflections from the concrete walls behind the Tx and Rx also contribute significant components. The pillars on the site (see Fig. 2) correspond to the other visible components. A lack of components in the rest of the APS shows that environmental objects other than building structures (such as vegetation) are not significant reflectors at the measured frequency. These result agree with the findings of [15], [16].

C. Angular spread

We expect angular spread to be small when Tx and Rx are close and for it to increase as the Rx moves away from the Tx. This is because the transmitted beam gets a chance to spread further from its central concentration as the link distance increases. From an elevation perspective, larger values should be expected where ϕ_{Rx} is other than 90° since the maximum LoS power concentration will be seen by the $\phi_{Rx} =$ 90° elevation cut. Table II summarizes the values for angular spread. The results we see therein are generally in line with the expectations we just discussed. We also note that while the angular spread for $\phi_{Rx} = 90°$ increases gradually as the distance increases from 1 to 2 to 5 m, the $d =$ 15 m case shows a significant jump. In this case, environmental objects surrounding the Rx such as pillars, and back walls have power

TABLE II: Angular Spread per location

Link Distance	1 m	2 m	5 m	15 m
$\phi_{\mathbf{Rx}} = \mathbf{80}^\circ$	0.18	0.24	0.32	0.73
$\phi_{\mathbf{Rx}} = \mathbf{90}^\circ$	0.14	0.21	0.29	0.75
$\phi_{\mathbf{Rx}} = \mathbf{100}^\circ$	0.17	0.23	0.3	0.68
$\phi_{\mathbf{Tx}} = \mathbf{90}^\circ$	0.2	0.24	0.38	0.57

levels comparable to the LoS power; something that is also visible in 4 (b).

D. RMS delay spread

For the RMS delay spread, the directions where the Tx and Rx are facing each other should show smaller values compared to other directions since they represent the smallest delay spread. Fig. 5 shows the values for RMS delay spread for all the azimuth directions when Rx is set at $\phi_{Rx} = 90^\circ$ for the $d =$ 1 m and $d =$ 15 m case. As anticipated, the LoS directions show the smaller values of RMS delay spread (approx. -85 dBs), whereas in other directions the values can be up to -65 dBs [1] Given the environment, Tx has a back wall at 3 m from it, therefore, a strong reflection is obtained when the Tx looks back and Rx looks towards Tx; this effect can also be observed in Fig. 4. For the case of $d =$ 15 m, given the fact that Tx and Rx are far away, the LoS contribution is reduced in comparison to the MPC as seen from the PDP in Fig. 3 (d). As a consequence, there are additional directions where the RMS delay spread shows small values, for example in $(\theta_{Tx} = 0^\circ, \theta_{Rx} = 180^\circ)$ (corresponding to the wall located behind the Rx).

E. Power distribution over MPCs and path loss

Path loss analysis for the route is shown in Fig. 6. For this analysis, the power of the LoS bin of the "best beam", the total power of the best beam, and the power of the omni-directional reconstruction are used to compute the path loss. As can be seen in Fig. 6, for the LoS bin case, the points are close to the free space path loss showing a root mean squared error (RMSE) lower than 1.81 dB. If we create a 3 sample window to capture the LOS power, the RMSE is reduced to 0.75 dB. The proximity between the points and free space path loss can be explained by the fact that the strongest components are contained in the horizontal plain ($\theta = 90^\circ$). The difference between the LoS bin and the omni-directional power is less than 3 dB, indicating that the LoS component dominates the total received power.

For the power distribution of the strongest MPCs, from physical considerations we know that the best beam case should give the higher concentration of power in the strongest MPCs as compared to the omni-directional case. This concentration reduces when the distance between Tx and Rx increases because a higher number of strong MPCs are observed at larger distances as seen in Fig. 3. Fig. 7 describes the distribution of power over the strongest MPCs, ($K =$ 1 is the LoS MPC). For $d =$ 1 m, the LoS MPC constitutes 95% of the total power for both the best beam and omni-directional cases, due to the relatively short link length. Comparing it against $d =$ 15 m, the concentration of power in the LoS MPC is reduced to 70% for omni-directional case due to a higher number of MPCs.

[1]The results are given on a dBs scale (as is common, e.g., in standardized channel models); the spread on a linear scale is $10^{x/10}$, i.e. -80 dBs corresponds to 10 ns.

IV. Conclusions

In this paper, we analyze the results of a double-directional channel measurement campaign conducted on a linear route in an urban environment at 140 GHz. Our results show how various channel parameters such as RMS delay spread, and angular spread change as the distance between the Tx and the Rx increases. In the case of the angular spread, the ratio between the beginning and the end of the route is approximately 5 times. For RMS delay spread, there is a strong correlation between the directions with high power and low delay spread. For short distances, low delay spread is highly concentrated in the LoS direction, however, as the Rx move away from the Tx, additional directions with lower delay spread can be identified. Path loss values show a close agreement with free space path loss for these measurements. Finally, the LoS MPC constitutes at least 70% of the total power and this ratio increases when the distance is lower. These results can offer insights into the design of future THz communication systems.

Acknowledgments

The work of USC was partly supported by the Semiconductor Research Corporation (SRC) under the ComSenTer program and by Samsung Research America. The work of J. Gomez-Ponce is partially supported by the Foreign Fulbright Ecuador SENESCYT Program.

References

[1] E. Dahlman, S. Parkvall, and J. Skold, *5G NR: The next generation wireless access technology*. Academic Press, 2020.

[2] K.-C. Huang and Z. Wang, "Terahertz Terabit Wireless Communication," *Microwave Magazine, IEEE*, vol. 12, no. 4, pp. 108–116, June 2011.

[3] A. Hirata and M. Yaita, "Ultrafast Terahertz Wireless Communications Technologies," *IEEE Transactions on Terahertz Science and Technology*, vol. 5, no. 6, pp. 1128–1132, Nov 2015.

[4] I. F. Akyildiz, J. M. Jornet, and C. Han, "TeraNets: ultra-broadband communication networks in the terahertz band," *IEEE Wireless Communications*, vol. 21, no. 4, pp. 130–135, August 2014.

[5] H. J. Song and T. Nagatsuma, "Present and Future of Terahertz Communications," *IEEE Transactions on Terahertz Science and Technology*, vol. 1, no. 1, pp. 256–263, Sept 2011.

[6] T. Kürner and S. Priebe, "Towards THz Communications - Status in Research, Standardization and Regulation," *Journal of Infrared, Millimeter, and Terahertz Waves*, vol. 35, no. 1, pp. 53–62, 2014.

[7] S. Kim and A. Zajić, "Characterization of 300-ghz wireless channel on a computer motherboard," *IEEE Transactions on Antennas and Propagation*, vol. 64, no. 12, pp. 5411–5423, 2016.

[8] N. A. Abbasi, A. Hariharan, A. M. Nair, and A. F. Molisch, "Channel measurements and path loss modeling for indoor thz communication," in *2020 14th European Conference on Antennas and Propagation (EuCAP)*. IEEE, 2020, pp. 1–5.

[9] H. Tataria, M. Shafi, A. F. Molisch, M. Dohler, H. Sjöland, and F. Tufvesson, "6g wireless systems: Vision, requirements, challenges, insights, and opportunities," 2020.

[10] FCC, "Fcc takes steps to open spectrum horizons for new services and technologies," http://https://docs.fcc.gov/public/attachments/DOC-356588A1.pdf, 2019.

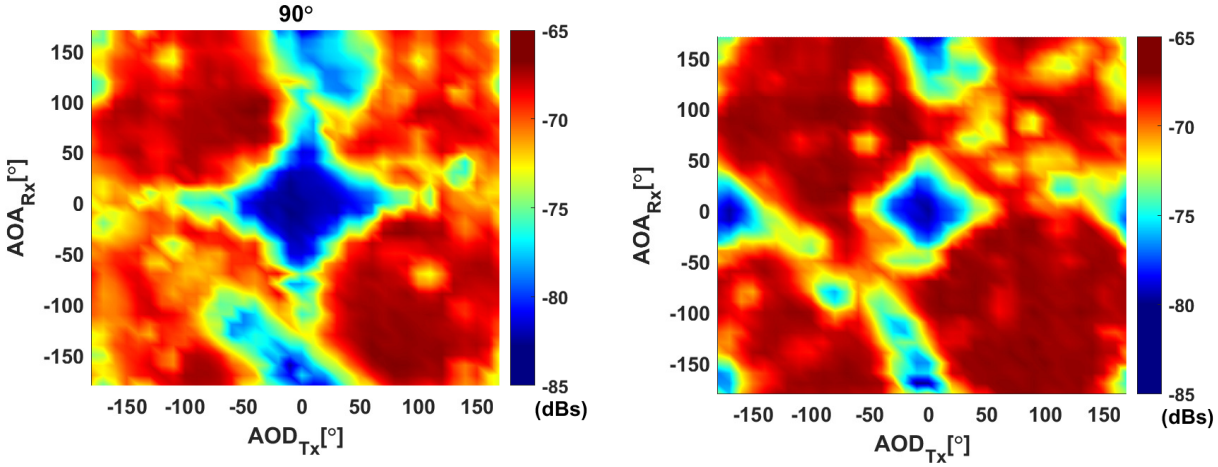

(a) 1 m.

(b) 15 m.

Fig. 5: RMS delay spread (in dBs) for $\phi_{Rx} = 90°$.

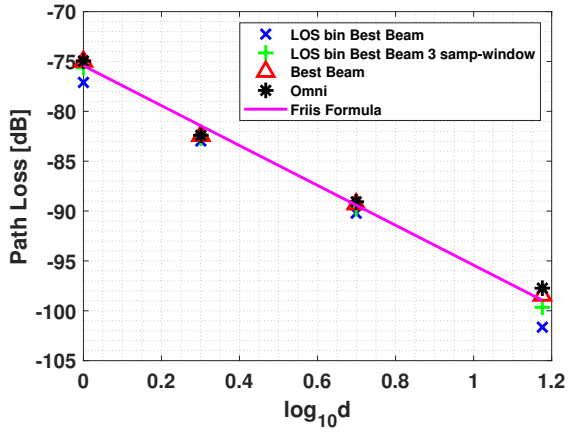

Fig. 6: Path loss comparison.

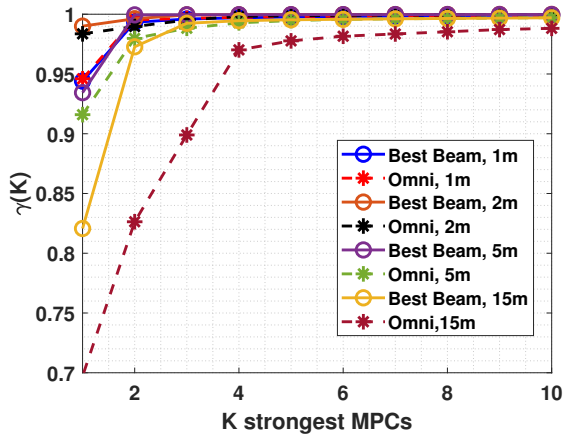

Fig. 7: Power distribution of the K strongest MPCs.

[11] M. Y.-W. Chia, B. Luo, and C. K. Ang, "Extremely wideband multipath propagation channel from 285 to 325 ghz for a typical desk-top environment," in *Infrared Millimeter and Terahertz Waves (IRMMW-THz), 2010 35th International Conference on*. IEEE, 2010, pp. 1–1.

[12] S. Priebe, C. Jastrow, M. Jacob, T. Kleine-Ostmann, T. Schrader, and T. Kürner, "Channel and propagation measurements at 300 GHz," *Antennas and Propagation, IEEE Transactions on*, vol. 59, no. 5, pp. 1688–1698, 2011.

[13] S. Kim and A. G. Zajić, "Statistical characterization of 300-ghz propagation on a desktop," *IEEE Transactions on Vehicular Technology*, vol. 64, no. 8, pp. 3330–3338, 2015.

[14] N. Khalid, N. A. Abbasi, and O. B. Akan, "Statistical characterization and analysis of low-thz communication channel for 5g internet of things," *Nano Communication Networks*, vol. 22, p. 100258, 2019.

[15] N. A. Abbasi, A. Hariharan, A. M. Nair, A. S. Almaiman, F. B. Rottenberg, A. E. Willner, and A. F. Molisch, "Double directional channel measurements for thz communications in an urban environment," in *ICC 2020-2020 IEEE International Conference on Communications (ICC)*. IEEE, 2020, pp. 1–6.

[16] N. A. Abbasi, J. Gomez-Ponce, S. M. Shaikbepari, S. Rao, R. Kondaveti, S. Abu-Surra, G. Xu, C. Zhang, and A. F. Molisch, "Ultra-wideband double directional channel measurements for thz communications in urban environments," in *ICC 2021-2021 IEEE International Conference on Communications (ICC)*. IEEE, 2021.

[17] M. Steinbauer, A. F. Molisch, and E. Bonek, "The double-directional radio channel," *IEEE Antennas and propagation Magazine*, vol. 43, no. 4, pp. 51–63, 2001.

[18] J. Gomez-Ponce, D. Burghal, N. A. Abbasi, A. Hariharan, G. Jakhetia, P. Chaganlal, and A. F. Molisch, "Directional delay spread and interference quotient analysis in sub-7ghz wi-fi bands," in *GLOBECOM 2020 - 2020 IEEE Global Communications Conference*, 2020, pp. 1–6.

[19] C. U. Bas, R. Wang, S. Sangodoyin, S. Hur, K. Whang, J. Park, J. Zhang, and A. F. Molisch, "28 ghz foliage propagation channel measurements," in *2018 IEEE Global Communications Conference (GLOBECOM)*, 2018, pp. 1–6.

[20] A. F. Molisch, *Wireless communications*. Wiley, 2011.

[21] B. H. Fleury, "First-and second-order characterization of direction dispersion and space selectivity in the radio channel," *IEEE Transactions on Information Theory*, vol. 46, no. 6, pp. 2027–2044, 2000.